Magnetoplasmonic coupling in graphene nanodisk dimers: An extended coupled-dipole model for circularly polarized states

Ningning Wang, Linhui Ding, and Weihua Wang [*]

School of Material Science and Physics, China University of Mining and Technology, Xuzhou 221116, People's Republic of China

Plasmonic coupling is one of the most important effects in compact plasmonic systems, and it has been studied intensively. In contrast, magnetoplasmonic coupling (MPC) is rarely mentioned, even in graphene nanostructures supporting the strong magneto-optic effect. Here, we theoretically investigate MPC in graphene nanodisk dimers in the presence of either parallel (case I) or antiparallel (case II) magnetic fields. We find the hybridized modes always appear for two states with same chirality, while their excitations depend on incident polarization. Moreover, two antisymmetric modes are dark in case I, but all four modes are bright in case II. To provide better insight, an extended coupled-dipole model is presented, in which the fundamental circularly polarized magnetoplasmons are decomposed into two linear and orthogonal dipoles, with a $\pi/2$ phase difference, and then the coupling is described by two linear dipoles along the two orthogonal directions separately. The parameters for the magneto-optic effect and coupling strengths are independent and can be easily extracted from their individual simulations. The eigenvalues and wave functions obtained from the model can describe well the resonance frequency and excitation strength of each hybridized mode. We finally discuss MPC in touching graphene nanodisks, where the charge transfer plasmon is immune to the magneto-optic effect, and in case II, a circular resonance state will be replaced by a linear one with the incident electric field along the touching direction. In this paper, we provide a general framework for investigating mode coupling of two circular states and pave the way to magneto-optic and plasmonic applications.

I. INTRODUCTION

Plasmonics, a rapidly developing field of optics beyond the diffraction limit [1–3], has been widely explored for decades in noble metals. It can serve as a bridge between photonics and electronics, thus holding the potential to design devices with both benefits [4–6]. However, the lack of dynamic tunability of metals hinders its further development. As an emerging two-dimensional (2D) material, graphene has attracted the great attention of the plasmonics community since it was isolated by mechanical exfoliation [7]. It has been demonstrated that graphene can be a promising platform for plasmonics, exhibiting active tunability through electrostatic gating [8], which is confirmed experimentally by near-field scattering microscopy [9,10]. Moreover, due to its excellent electronic properties, the supporting plasmonic resonances show better performance in confinement, enhancement, and lifetime [11–13]. Graphene plasmonics opens an avenue toward the active manipulation of light-matter interaction at the nanoscale, which enables the manufacture of compact optical devices with functionalities, especially working at terahertz and infrared regimes [14–16]. Meanwhile, with the rise of this field (also known as 2D flatland optics [17]), the study of even more 2D materials, such as molybdenum disulfide [18], transition metal dichalcogenides [19], and black phosphorus [20], has drawn widespread interest.

In plasmonic nanostructures, multiple elements are usually designed compactly in a single unit cell, in which plasmonic coupling is inevitable and even plays an important role in engineering required functionalities and broad bandwidth. On the other hand, plasmonic coupling has received its own interest in the study of physics phenomena in optical systems, e.g., Fano resonance [21–23], electromagnetically induced transparency [24–26], and bound states in continuum [27–29]. However, authors of most of these studies consider only the coupling effects between the modes carrying linear momenta, such as that of dipole-dipole [30–32], dipole-multipole [33], and multipole-multipole [34]. Discussion of coupling between the modes with angular momenta (e.g., circularly polarized states) is generally lacking. In graphene, it is easy to encounter such coupling since the strong magneto-optical response can be seen as a direct consequence of its electronic structures (e.g., well-separated Landau levels). Accordingly, the quantum Hall effect can be measured even at room temperature [35–37], whereas this was previously only possible at liquid-helium temperatures [38]. In the presence of magneto-optic effects, the plasmonic resonance in graphene will be strongly modified to show mode splitting and angular momentum [39–41]. This collective excitation of free electrons/holes in cyclotron motion is usually termed a *magnetoplasmon* (MP). Comparing with the electric field, the magnetic field provides a different manner to actively tune graphene plasmons, through changing the motion of the carrier rather than its concentration. Although MPs have been studied in various nanostructures of graphene [42–44], the

[*]wh.wang@outlook.com

magnetoplasmonic coupling (MPC) effects are usually not considered.

In this paper, we theoretically investigate MPC in graphene nanodisk dimers in the presence of either parallel (case I) or antiparallel (case II) magnetic fields. As usual, the full wave simulations are carried out by modeling graphene as a very thin three-dimensional (3D) film, characterized by in-plane magneto-optical conductivity. We show that the extinction of such magnetoplasmonic dimers is also attributed to the typical symmetric and antisymmetric modes, which can be regarded as the combination of MPs with the same chirality. However, two antisymmetric modes are dark in case I, while they turn to be bright in case II. In both cases, the mode excitation relies on incident polarization, e.g., parallel or perpendicular to the dimer. We find such MPC effects can be well described by an extended coupled-dipole model, generally applicable to any circularly polarized oscillators, in which a circular MP on each nanodisk is presented by two orthogonal linear dipoles with a $\pi/2$ phase difference. By merging the straight dipole-dipole coupling between the two nanodisks, a 4×4 Hamiltonian is formulated, from which the eigenresonance frequencies are in good agreement with those from simulations. Meanwhile, the wave functions can also be used to predict the excitation strength of each hybridized mode in both cases. Finally, MPC in nanodisk dimers of limited condition (the touching nanodisks), is also discussed, in which some hybridized modes are seen to exhibit strong suppression of magneto-optic effects.

II. OPTICAL RESPONSE OF GRAPHENE

Despite being a 2D material, the optical response of graphene can be treated macroscopically through its frequency-dependent surface conductivity $\sigma(\omega)$. In general, $\sigma(\omega)$ can be derived within the framework of linear response theory (equivalently random phase approximation) by considering both intraband and interband transitions. However, for low-energy excitations, the intraband transition dominates, and then $\sigma(\omega)$ can be reduced to a simple Drude formula [45–47]. In the presence of a magnetic field, a similar treatment can be implemented at the limit of high doping, e.g., considering only the Landau levels around the Fermi level [48–50]. In this instance, the magneto-optical conductivity $\sigma(\omega)$ of graphene will take a similar formula as that of traditional 2D electron gases [44], which has been adopted throughout this paper. To carry out 3D simulations, we follow the common practice to model graphene as a very thin film with an artificial thickness t_g (0.5 nm throughout this paper), and then the in-plane components ε_{in} of the effective 3D dielectric function $\varepsilon(\omega)$ can be represented as

$$\varepsilon_{\text{in}}(\omega) = \varepsilon_0 + \frac{i}{\omega t_g} \begin{bmatrix} \sigma_{xx}(\omega) & \sigma_{xy}(\omega) \\ \sigma_{yx}(\omega) & \sigma_{yy}(\omega) \end{bmatrix}, \quad (1)$$

while the other off-diagonal components of $\varepsilon(\omega)$ are simply zero and $\varepsilon_{zz}(\omega) = \varepsilon_0$. The Drude formula of the conductivity terms in parentheses can be expressed by

$$\sigma_{xx}(\omega) = \sigma_{yy}(\omega) = \frac{e^2 \mu_c}{\pi \hbar^2} \frac{i(\omega + i\tau^{-1})}{(\omega + i\tau^{-1})^2 - \omega_c^2},$$

$$\sigma_{xy}(\omega) = -\sigma_{yx}(\omega) = \frac{e^2 \mu_c}{\pi \hbar^2} \frac{\omega_c}{(\omega + i\tau^{-1})^2 - \omega_c^2}. \quad (2)$$
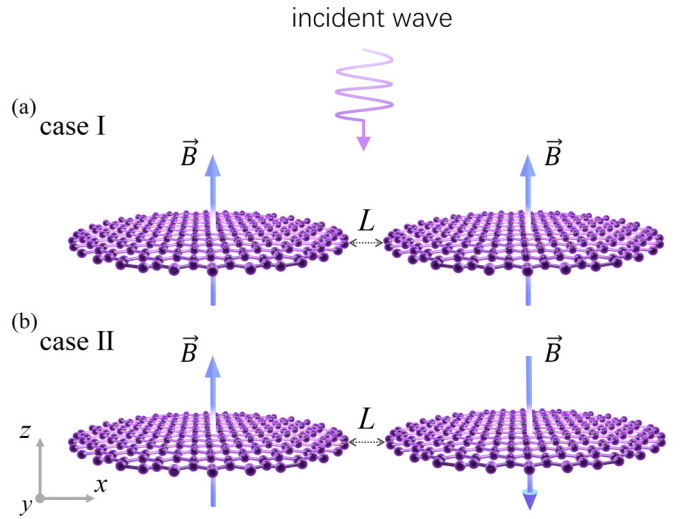

FIG. 1. Schematic diagram of the graphene nanodisk dimer in the presence of (a) parallel and (b) antiparallel magnetic fields. The dimer consists of two identical nanodisks of 50 nm radius and separated by a distance L.

Here, μ_c is the chemical potential, which is set as a constant value 0.6 eV throughout this paper, τ is the intrinsic relaxation time defined as $\tau = \mu \mu_c / e v_F^2$ (in graphene, the charge carrier mobility $\mu = 10^4$ cm^2/Vs, and Fermi velocity $v_F = 10^6$ m/s), and $\omega_c = eB/m^* = eB v_F^2/\mu_c$ is the cyclotron resonance frequency. The dependence of Drude weight $D = e^2 \mu_c/\hbar^2$ on the Planck constant and that of effective mass $m^* = \mu_c/v_F^2$ on chemical potential originate exactly from the nature of Dirac fermions, which are different from those in 2D electron gases with parabolic energy dispersion. Since it is linearly proportional to B/μ_c, the cyclotron frequency ω_c determining the strength of magneto-optic effects can be tuned actively through both magnetic and electric fields.

III. RESULTS AND DISCUSSION

A. MPC in graphene nanodisk dimers

We now study the optical excitations of graphene nanodisk dimers in the presence of two perpendicular magnetic fields that are either parallel (case I) or antiparallel (case II), as shown in Fig. 1. It is worth noting that, in case II, the magnetic field changes its direction over a few nanometers as the separation $L \to 0$. This is a practical issue for fabrication, which might be treated by using the technique proposed recently [51]. Under the normal incidence of a plane wave with electric field $\vec{E} = \vec{E}_0 \exp[i(k_0 z - \omega t)]$, the extinction efficiency can be calculated by implementing the optical theorem, which can be written as [52,53]

$$\sigma_{\text{ext}} = \frac{4\pi}{S k_0} \frac{\text{Im}\{\vec{E}_0^* \cdot \vec{F}(\vec{k} = k_0 \hat{z})\}}{|\vec{E}_0|^2}, \quad (3)$$

where S is the cross-section of the nanostructure, k_0 is the wave vector in free space, $\vec{E}_0$ is the incident amplitude, and $\vec{F}(\vec{k})$ is the scattering amplitude of the electric far field evaluated in the forward direction (along the incident wave

vector), with its component along the incident polarization vector extracted from the product $\vec{E}_0^* \cdot \vec{F}(\vec{k})$. According to the definition, the relationship between the scattering amplitude $\vec{F}(\vec{k})$ and the electric far field $\vec{E}_{\mathrm{far}}(\vec{k})$ is simply given by

$$\vec{E}_{\mathrm{far}}(\vec{k}) = \frac{e^{ikr}}{r}\vec{F}(\vec{k}).$$

To obtain this scattering amplitude $\vec{F}(\vec{k})$, the full-wave simulations are carried out by using the commercial finite element method package COMSOL MULTIPHYSICS. In practice, the nanodisk dimer is placed at the center of a computational domain truncated by a perfect match layer, and the forward scattering amplitude $\vec{F}(\vec{k} = k_0\hat{z})$ can be directly extracted from the built-in function. Note that, in COMSOL, the variable *Efar* used for far field calculation is exactly the scattering amplitude $\vec{F}(\vec{k})$ rather than $\vec{E}_{\mathrm{far}}(\vec{k})$. To identify the plasmonic resonance modes, the field pattern (E_z field distribution) at each resonance frequency will be plotted at 1 nm above the disks, and by monitoring its time evolution, the oscillating path of each mode can be obtained.

Because of the very small thickness of graphene nanodisks, the convergence of COMSOL simulations is a typical issue that needs to be treated carefully. In principle, fine meshing is required to resolve the nanodisks and guarantee numerical precision. For the dimers studied below, the separation between two graphene nanodisks varies from tens of nanometers to zero (touching case), in which the meshing would be even more crucial. To make the simulation results reliable, a convergence check has been conducted for each dimer. Specifically, the quality of the mesh element in COMSOL can be customized by two variables, the maximum and minimum element sizes, and by tuning them gradually, the numerical convergence of those simulations can be easily verified. For simplicity, the detailed convergence tests of several typical cases are summarized in the Appendix. It is seen that, in those figures, the convergence results are achieved, as shown by the green curves, for which the mesh setting is used in the studies below.

To proceed, we first calculate the extinction spectra of the dimer of distance $L = 20$ nm and radius $R = 50$ nm for each nanodisk. Since changing the radius will cause a global shift of resonance frequency, e.g., yielding a simple scaling law [30,54,55], the coupling behavior for different radii is very similar. Thus, without loss of generality, a constant radius is used in this paper. The simulation results are shown in Fig. 2, and for purposes of comparison, that of an individual nanodisk is also present in Fig. 2(a). As we know, in the presence of a magnetic field, the linearly polarized and doubly degenerate dipole mode in a nanodisk (peak at the black curve) will undergo symmetrical mode splitting (peaks at the red curve). The two emerging resonance states carry the right-handed/left-handed circular polarization (RHCP/LHCP), as shown by the inset. Here, the double degeneracy is crucial for the phenomenon, e.g., as in the absence of this degeneracy, the mode splitting will disappear [40]. It is very easy to think of the coupling between these two circularly polarized states, which should be fundamentally different from that of two linearly polarized states.
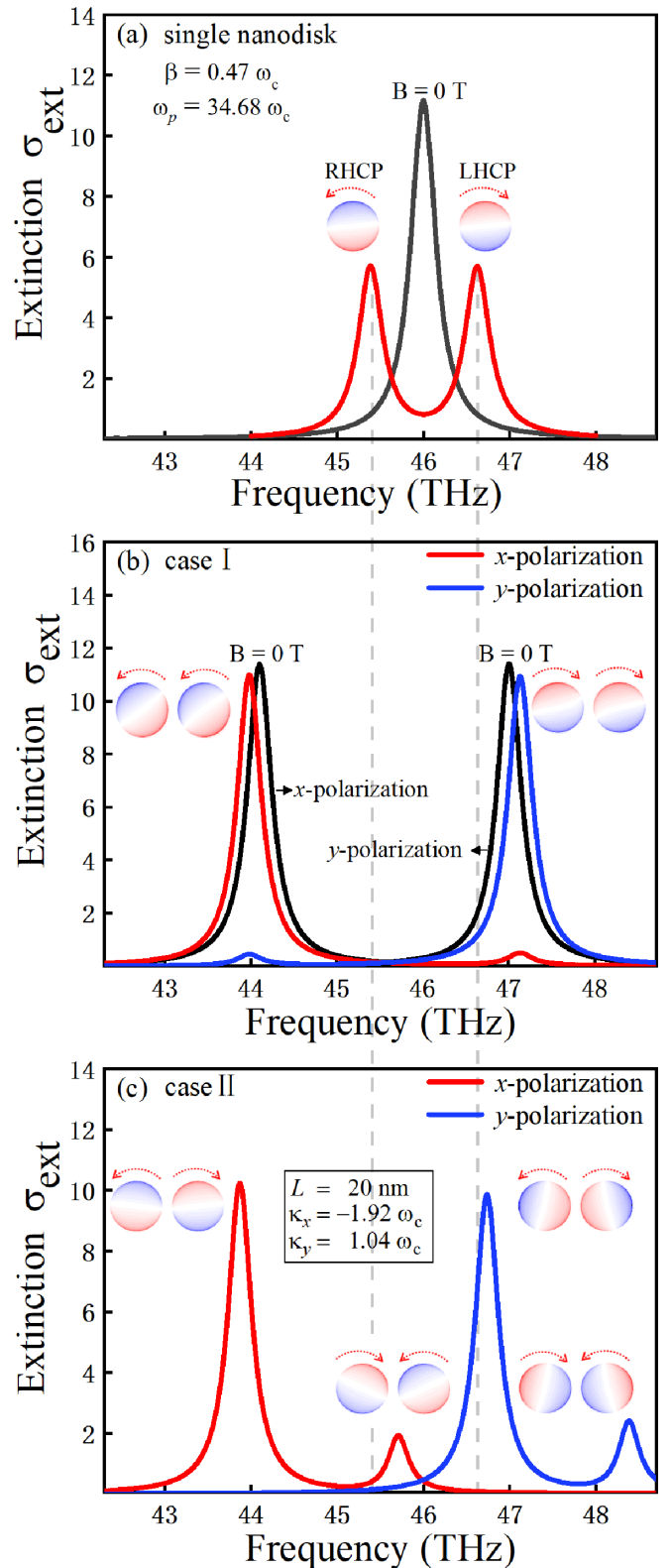

FIG. 2. Extinction spectra of a single graphene nanodisk and the dimer in cases I and II. The black curves in (a) and (b) are the extinction of the nanodisk and the dimer as $B = 0$ T, respectively. The insets show the field patterns of each hybridized mode and the values of κ_x and κ_y. The two dotted curves mark the resonance frequencies of two circular magnetoplasmons (MPs) of right-handed circular polarization (RHCP) and left-handed circular polarization (LHCP), respectively.

In graphene nanodisk dimers, the extinction spectrum will be different for different magnetic field layouts and incident polarizations. In case I, there is a dominating resonance peak in the spectra of both polarizations [curves in Fig. 2(b)] yet at different frequencies. For *x* polarization, the resonance mode can be regarded as the hybridized mode of two RHCP states (see insets), while for *y* polarization, the resonance mode is a combination of two LHCP states. Like the coupling in linear polarizations, the coupling here will cause a blueshift of LHCP and a redshift of RHCP. Because of the orthogonality of two wave functions, the cross-coupling between the states of RHCP and LHCP is prohibited. It is also noted that two small peaks exist with frequencies and wave functions identical to those of the major peaks. This indicates only two hybridized modes are present here, which possess different overlapping functions from the external excitation of different polarizations. From the general coupling picture, they are both symmetrically hybridized, while the antisymmetric modes are completely absent (dark). Comparing the resonances with *B* = 0 T (black curve), the state of RHCP is redshifted, while that of LHCP is blueshifted. In case II, the extinction spectrum of each polarization is also dominated by a major resonance peak, which is always the lower energy one. Meanwhile, the small peaks are more pronounced than those in case I and do not possess identical frequencies to those of major resonances. Here, four (rather than two) hybridized modes appear, which can be thought of as a direct consequence of the inversion symmetry breaking caused by the antiparallel magnetic fields. However, as shown by the insets, their wave functions seem not to be the pairs of two states of either RHCP or LHCP, e.g., different rotation directions on two nanodisks. Specifically, two major resonances are a combination of two states rotating anticlockwise and clockwise, respectively, which behave like the cross-coupling between the states of RHCP and LHCP. To understand the observation, we must recognize the origin of wave rotation, namely, the charge carrier cyclotron resonance. Therefore, to determine the chirality of each state, the external magnetic field will be the rotating axis naturally. Then it is easy to find that the right one carries also RHCP since the magnetic field is in the opposite direction [see Fig. 1(b)]; thus, accordingly, they are hybridized modes of RHCP. To classify them, we further examine their wave functions and find a π phase difference between two rotations in *y* polarization. The two major resonances are symmetrically (lower energy) and antisymmetrically (higher energy) hybridized, with none of them dark, which is significantly different from case I. The same analysis can also be applied to the two minor resonances, which are symmetrically (lower energy) and antisymmetrically hybridized modes of LHCP.

B. Mode decomposition and coupled-dipole model

To understand the above observations, exploring the implicit coupling mechanism between two circularly polarized states is of crucial importance. As we know, the coupling between two linearly polarized states has been well studied, which can be formalized as an empirical coupled-oscillator theory, with a parameter κ generally used to describe the coupling strength [30,31,33]. If the two states have resonance frequencies ω_a and ω_b, respectively, it is easy to write the
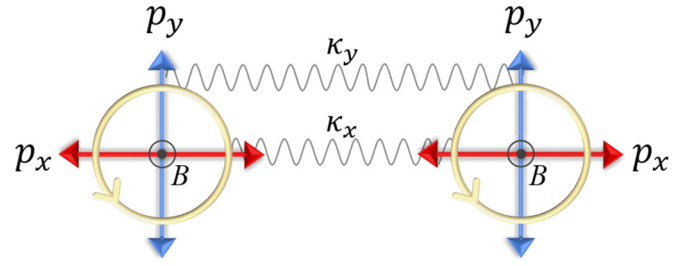

FIG. 3. Schematic diagram of the extended coupled-dipole model. The circular magnetoplasmons (MPs; yellow rings) are decomposed into two orthogonal and linear dipoles (red and blue arrows), with a $\pi/2$ phase difference. The wavy lines depict the coupling of two dipoles of *x* polarization (κ_x) and *y* polarization (κ_y).

Hamiltonian of the coupled system, for example, as

$$H = \begin{pmatrix} \omega_a & \kappa \\ \kappa & \omega_b \end{pmatrix}.$$

Diagonalization of *H* will give the frequencies of symmetric and antisymmetric states and their wave functions which are a linear superposition of the wave functions of states *a* and *b*. The theory is constructed from a perturbation framework, which requires a weak coupling, e.g., the wave functions strongly bounded to the oscillators. In plasmonics, due to extreme field localization, the theory is generally valid and works even better in graphene nanostructures. Thus, we adopt the theory in this paper as well. However, because of the circularly polarized states, the direct application is impossible, and a specific treatment should be incorporated. Inspired by our previous work [56], a perfect circularly polarized state was decomposed into two orthogonal linearly polarized states yet with a $\pi/2$ phase difference. Here, the fundamental states are linear dipole resonances $\vec{p}_x$ and $\vec{p}_y$, so the circular dipole resonances are $\vec{p}_{R/L} = \vec{p}_x \pm i\vec{p}_y$, which result in the radiation of RHCP and LHCP waves. Based on this decomposition, it can formulate an extended coupling theory for circular states.

For two linear dipoles $\vec{p}_a$ and $\vec{p}_b$, the coupling strength κ is proportional to a volume integral $\int \vec{p}_a \cdot \vec{E}_b^* dV$, where $\vec{E}_b$ is the local field generated by $\vec{p}_b$ at the position of $\vec{p}_a$. Here, $\vec{E}_b$ is determined by $\vec{p}_b$, e.g., approximately $\vec{E}_b \propto \vec{p}_b / R^3$, with *R* the separation of two dipoles. In this sense, for point dipoles, κ is proportional to $\vec{p}_a \cdot \vec{p}_b^* / R^3$ or simply $\vec{p}_a \cdot \vec{p}_b^*$, supposing a constant separation. It is usual to consider two basic cases, namely, two horizontal dipoles ($\kappa_x \propto p_x p_x^*$, the subscripts *a* and *b* are omitted for simplicity) or two vertical dipoles ($\kappa_y \propto p_y p_y^*$), where κ_x and κ_y are often unequal. Following this strategy, we investigate the coupling of two circular dipoles $\vec{p}_{R/L}$. Similarly, the coupling strength is taken as $\kappa \propto \vec{p}_{R/L} \cdot \vec{p}_{R/L}^*$, while by incorporating the decomposition, we can easily obtain $\kappa \propto p_x p_x^* + p_y p_y^*$. Here, it is quite impressive that the coupling of two circular states can be represented by a linear combination of the coupling of two linear states. Such an extended model can be summarized and shown intuitively in Fig. 3 (case I as an example), where the coupling between p_x and p_y in each resonance is induced by the magneto-optic

effect, and the coupling between two resonances is determined by κ_x and κ_y. Accordingly, the Hamiltonian of this coupled system can be derived readily from the above Hamiltonian, which is

$$H_\pm = \begin{bmatrix} \omega_p - i\gamma & i\beta & \kappa_x & 0 \\ -i\beta & \omega_p - i\gamma & 0 & \kappa_y \\ \kappa_x & 0 & \omega_p - i\gamma & \pm i\beta \\ 0 & \kappa_y & \pm(-i\beta) & \omega_p - i\gamma \end{bmatrix}, \quad (4)$$

with the sign $\pm$ indicating cases I and II, respectively, and γ the phenomenological damping of MPs. It is seen that the submatrices in top left and bottom right corners describe magnetoplasmonic resonances at each nanodisk, e.g., the resonance frequencies (the real part of the eigenvalues) satisfying $\omega_p \pm \beta$, corresponding to LHCP and RHCP, respectively. In practice, β can be easily extracted from Fig. 2(a), which is roughly $\omega_c/2$ in circular nanodisks. On the other hand, as in the absence of a magnetic field, the resonance frequencies of two coupled linear states are either $\omega_p \pm \kappa_x$ or $\omega_p \pm \kappa_y$, which are identical to those from Eq. (4) and used to extract the values of κ_x and κ_y.

Moreover, it is worth noting that the term $-i\gamma$ in Eq. (4) is well separated from other terms. In other words, each complex eigenvalue of the Hamiltonian can always be expressed as a real component and an imaginary component $-i\gamma$. This means the coupling effect acts mostly on the real component, namely, resonance frequency. Generally, the value of γ consists of the contributions from dissipative and radiative losses, which are determined by intrinsic relaxation time τ [see Eq. (2)] and photon radiation [57], respectively. In graphene plasmonic systems, because of the tightly bounded feature of resonance modes, the dissipative loss dominates [58]. Hence, when a constant τ is used throughout this paper, it is not difficult to imagine that magnetoplasmonic damping remains almost unchanged. In practice, the value of γ can be obtained by directly carrying out eigenvalue calculation in simulations or calculated from the full width at half maximum of the resonance peaks in extinction spectra. By adopting the modeling used in Fig. 2, eigenvalue calculation gives $\gamma = 0.085\omega_c$ in a single graphene nanodisk, and when $B = 5$ T, $\gamma = 0.083\omega_c$ and $0.086\omega_c$ for the states of RHCP and LHCP, respectively; in case I, $\gamma = 0.092\omega_c$ and $0.095\omega_c$ for the lower and higher frequency hybridized modes, respectively; in case II, $\gamma = 0.091\omega_c$, $0.096\omega_c$, $0.093\omega_c$, and $0.095\omega_c$ for the four modes with resonance frequency from low to high, respectively. It is seen that the variation of γ is negligible since $\omega_c = 1.326$ THz is much smaller than the resonance frequency of each mode, e.g., $\omega_c \approx 0.03\omega_p$. Thus, for simplicity, we focus on the real component of the eigenvalues (resonance frequency) in the following discussion.

1. Resonance frequencies and wave functions in case I

To diagonalize the Hamiltonian $H_\pm$, it can obtain resonance frequencies and wave functions of those hybridized modes in such coupled systems. In case I [see Fig. 1(a)], the resonance frequencies are

$$\omega_{uv} = \omega_p \mp \tfrac{1}{2}\sqrt{4\beta^2 + (\kappa_x - \kappa_y)^2} \pm \tfrac{1}{2}(\kappa_x + \kappa_y), \quad (5)$$

where the first sign $\mp$ is for RHCP and LHCP (index $u = $ R or L), respectively, and the second sign $\pm$ is for symmetric and antisymmetric mode (index $v = $ S or A), respectively. The corresponding wave functions for RHCP are

$$\psi_{\mathrm{RS|RA}} = \begin{pmatrix} \eta_{\mathrm{R}} \\ i \\ \pm\eta_{\mathrm{R}} \\ \pm i \end{pmatrix}, \quad (6)$$

with a positive auxiliary parameter

$$\eta_{\mathrm{R}} = \frac{1}{2\beta}[\sqrt{4\beta^2 + (\kappa_x - \kappa_y)^2} \mp (\kappa_x - \kappa_y)],$$

and for LHCP are

$$\psi_{\mathrm{LS|LA}} = \begin{pmatrix} \eta_{\mathrm{L}} \\ -i \\ \pm\eta_{\mathrm{L}} \\ \mp i \end{pmatrix}, \quad (7)$$

with a positive auxiliary parameter

$$\eta_{\mathrm{L}} = \frac{1}{2\beta}[\sqrt{4\beta^2 + (\kappa_x - \kappa_y)^2} \pm (\kappa_x - \kappa_y)].$$

It is easy to find that, if $\kappa_x = \kappa_y = \kappa$, the two kinds of interactions will work independently, e.g., the frequencies $\omega_{uv} = \omega_p \mp \beta \pm \kappa$, in the absence of the cross-term. Meanwhile, the two wave functions are reduced to the linear combination of two exact circular states of RHCP or LHCP. However, due to their different dipole orientations, κ_x and κ_y always have different values and are opposite in sign, where $\kappa_x \leqslant 0$ and $\kappa_y \geqslant 0$ [30,31,59]. This indicates the only condition for $\kappa_x = \kappa_y$ is that they are both zero, namely, at a sufficiently large separation ($L \to \infty$). Otherwise, the interplay between these two kinds of coupling channels [the second term in Eq. (5)] is always present.

2. Resonance frequencies and wave functions in case II

Similarly, in case II [Fig. 1(b)], the resonance frequencies can be readily written as

$$\omega_{uv} = \omega_p \mp \tfrac{1}{2}\sqrt{4\beta^2 + (\kappa_x + \kappa_y)^2} \pm \tfrac{1}{2}(\kappa_x - \kappa_y), \quad (8)$$

with the indices u and v and the signs $\mp$ and $\pm$ share the same definitions as those in Eq. (5). Accordingly, the wave functions for RHCP are

$$\psi_{\mathrm{RS|RA}} = \begin{pmatrix} \eta_{\mathrm{R}} \\ i \\ \pm\eta_{\mathrm{R}} \\ \mp i \end{pmatrix}, \quad (9)$$

with

$$\eta_{\mathrm{R}} = \frac{1}{2\beta}[\sqrt{4\beta^2 + (\kappa_x + \kappa_y)^2} \mp (\kappa_x + \kappa_y)],$$

and for LHCP are

$$\psi_{LS|LA} = \begin{pmatrix} \eta_L \\ -i \\ \pm\eta_L \\ \pm i \end{pmatrix}, \tag{10}$$

with

$$\eta_L = \frac{1}{2\beta}[\sqrt{4\beta^2 + (\kappa_x + \kappa_y)^2} \pm (\kappa_x + \kappa_y)].$$

It is very interesting to see that both the resonance frequencies and wave functions are very similar in cases I and II. For instance, by simply replacing κ_x by $-\kappa_x$ (or κ_y by $-\kappa_y$), the resonance frequencies are the same, and the wave functions exhibit the only difference in the signs of the last component. It is also worth noting that, in both cases, the two modes with the same chirality (the same index u) will have their frequency difference determined by the third term, a straight dipole-dipole coupling term; on the contrary, with the same symmetry (the same index v), their frequency difference will be given by the second term, a cross-term. Moreover, κ_x and κ_y always appear in pairs, e.g., $\kappa_x + \kappa_y$ and $\kappa_x - \kappa_y$, which then contribute to the cross-term and dipole-dipole coupling term separately, and only the pair shown in the cross-term will emerge in the wave functions. As discussed above, in case II, $\kappa_x = -\kappa_y$ (disappearance of the cross-term) can only be satisfied when the separation is sufficiently large ($L \to \infty$).

3. Numerical investigations

To verify such an empirical model, we first investigate MPC under a constant magnetic field $B = 5$ T ($\beta = 0.47\omega_c$) and varying separation L. As shown by the insets in Fig. 4, the resonance peaks in both cases occur roughly at the frequencies indicated by the dashed lines, which are calculated from Eqs. (5) and (8). With increasing L, a better agreement is achieved, between the model (curves) and simulations (dots), and the resonances in both cases exhibit a redshift for two higher energy branches yet a blueshift for two lower energy branches, which is a clear repulsive effect in coupling systems. The largest and smallest energy branches are always ω_{LA} and ω_{RS}, respectively, but the other two branches are different. In case I, ω_{LS} is larger than ω_{RA}, and ω_{LS} (ω_{RA}) will merge with ω_{LA} (ω_{RS}) quickly, and finally, the energy gap between them remains at the value of 2β (approaching the limit of $\kappa_x = \kappa_y = 0$, e.g., at $L = 50$ nm). In case II, ω_{LS} is smaller than ω_{RA} at smaller separation and becomes larger than ω_{RA} as $L > 50$ nm. We find here the merging of symmetric and antisymmetric modes is much slower than that in case I, which means the straight dipole-dipole coupling decays slowly in this case.

Another significant difference between these two cases is the resonance strength of each hybridized mode. In case I, two antisymmetric modes ω_{RA} and ω_{LA} are completely dark; mode ω_{RS} dominates the excitation spectrum with x-polarized incidence, while mode ω_{LS} dominates for y-polarized incidence. In case II, none of them are dark; for x-polarized incidence, mode ω_{RS} is stronger than mode ω_{LS}, and for y-polarized incidence, mode ω_{RA} is stronger than mode ω_{LA}. In principle, these observations should be connected to the wave function
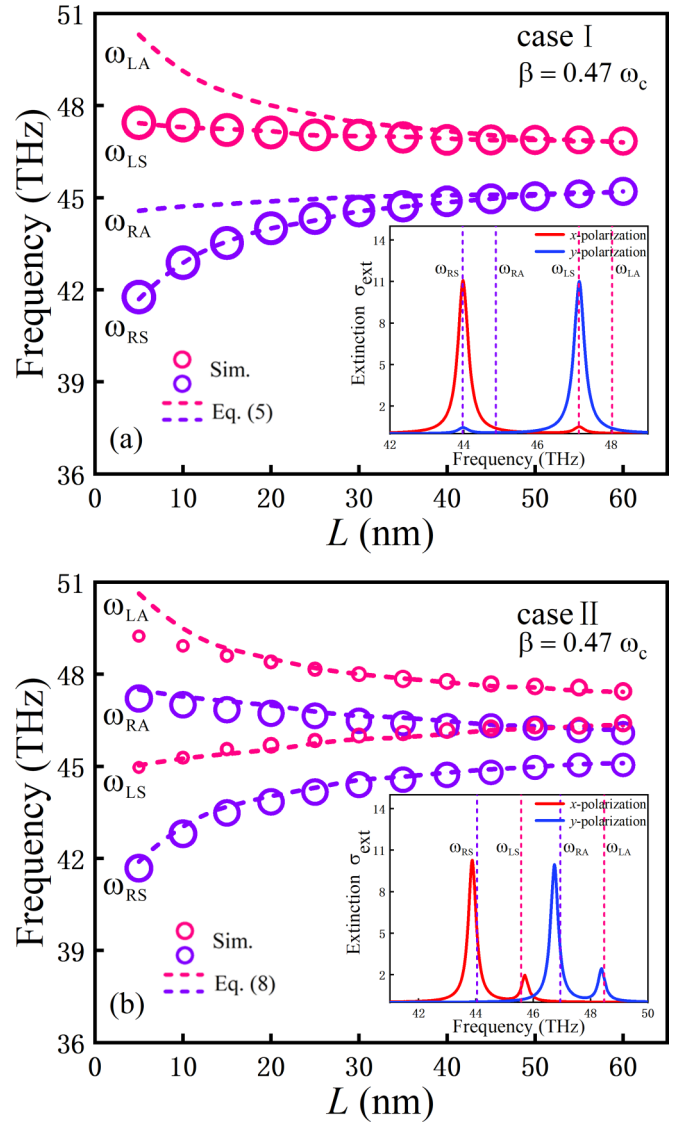

FIG. 4. Resonance frequencies of symmetric and antisymmetric modes as a function of the separation at a constant magnetic field $B = 5$ T. The circles and dashed curves are obtained from simulation and the model, respectively. The sizes of the circles represent the relative height of each peak. The inset shows a detailed comparison between the model and simulation at $L = 20$ nm.

of each mode. The second and fourth components are quite simple, e.g., either i or $-i$, corresponding to the y field distributed at the right and left nanodisks, respectively. In turn, the first and third components correspond to the x field that can be evaluated by directly substituting the values of the three parameters in η_R and η_L. Naturally, they are varied but are always positive, which gives the symmetry of each wave function and can be used to determine the mode excitation. In case I, it is seen that, for ψ_{RS} and ψ_{LS}, both electric and magnetic fields are in phase (carrying the same sign), which means they can be excited by x- and y-polarized incidence; for ψ_{RA} and ψ_{LA}, both electric and magnetic fields are out of phase (carrying the opposite signs), indicating darkness under any linearly polarized incidence. Considering $\kappa_x \leqslant 0$ and $\kappa_y \geqslant 0$, η_R for ψ_{RS} is much larger than η_L for ψ_{LS}, e.g.,

$\eta_R = 5.0$ and $\eta_L = 0.2$ at $L = 20$ nm; thus, for x-polarized incidence, the resonance strength of ψ_{RS} is much stronger. For y-polarized incidence, they seem to have the same imaginary unit, but if the normalization is present for the x field, it is quite easy to find the y field of ψ_{LS} is much larger than that of ψ_{RS}.

In case II, each wave function has an odd number of minus signs, which is completely different from that in case I, with an even number of minus signs. A significant consequence will raise up since the only opposite sign cannot make a dark mode in both directions and will make each mode only excited by one polarization. For ψ_{RS} and ψ_{LS}, the electric field is in phase, but the magnetic field is out of phase; it is just the opposite for ψ_{RA} and ψ_{LA}. Such a simple argument is exactly consistent with the simulations. To further investigate the relative resonance strength, the actual values of η_R and η_L are required. For example, $\eta_R = 2.0$ for ψ_{RS} is larger than $\eta_L = 0.5$ for ψ_{LS} at $L = 20$ nm, which corresponds to a stronger resonance of ψ_{RS}; while $\eta_R = 0.5$ for ψ_{RA} is smaller than $\eta_L = 2.0$ for ψ_{LA}, corresponding to a stronger resonance of ψ_{RA}.

To further confirm the validity of the model, we investigate here another situation, when the separation is fixed ($L = 50$ nm) and the magnetic field (B) is varied. As mentioned above, in case I, the symmetric and antisymmetric modes are roughly merged with a tiny constant energy difference given by $\kappa_x + \kappa_y = 0.03\,\omega_c$ [see Eq. (5)]. As shown in Fig. 5(a), a larger magnetic field will cause a larger energy difference between the modes with different chirality, a typical repulsive effect in coupling systems. It is also easy to find that they are roughly symmetrically distributed with respect to the frequency ω_p, as indicated by the dashed line. In case II, the observation is quite different, as shown in Fig. 5(b). With increasing the magnetic field, ω_{LA} and ω_{LS} increase almost linearly, with a constant energy difference given by $\kappa_y - \kappa_x = 0.99\,\omega_c$; meanwhile, ω_{RA} and ω_{RS} decrease almost linearly, with a $0.99\,\omega_c$ energy difference. The average frequency of two antisymmetric modes is $\omega_p - (\kappa_x - \kappa_y)/2$, as indicated by the upper dashed line, and that of two symmetric modes is $\omega_p + (\kappa_x - \kappa_y)/2$, as indicated by the lower dashed line. The approximate linear relation here is a direct consequence of $\kappa_x + \kappa_y \to 0$, which is included in the cross-term in case II. We find, with increasing the separation (equivalently $\kappa_x + \kappa_y \to 0$), the two cases exhibit different behaviors, which are clearly presented by the model, e.g., the merging of symmetric and antisymmetric modes in case I and the disappearance of the interplay between these two kinds of coupling channels in case II.

C. MPC in touching graphene nanodisks

Regarding a graphene nanodisk dimer, there exist two cases which correspond to two nanodisks far away from each other ($L \to \infty$) and touching ($L = 0$ nm). As $L \to \infty$, it is quite clear that the dimer will be reduced to two individual nanodisks without coupling, namely, $\kappa_x = \kappa_y = 0$. Thus, the optical excitation will be solely determined by the magneto-optic effect, the same as that shown in Fig. 2(a). It is also interesting to explore the behavior at the other limit as $L = 0$ nm, which is so far not transparent to us. Therefore, we study here the MPC in touching graphene nanodisks. For compar-
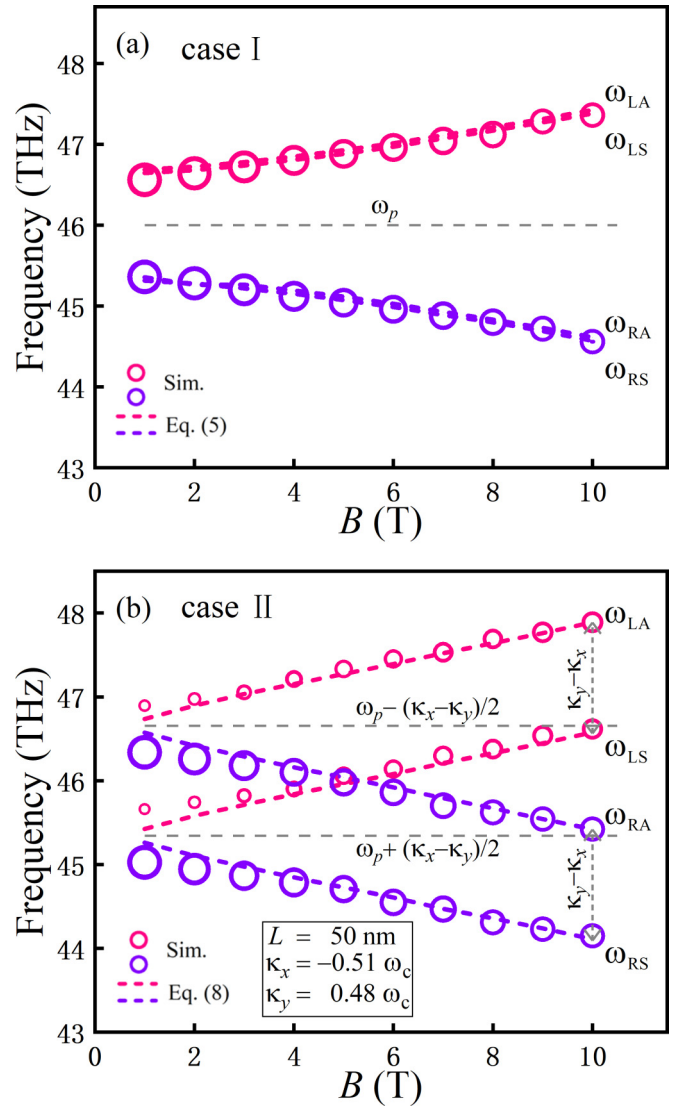

FIG. 5. Resonance frequencies of symmetric and antisymmetric modes as a function of magnetic field at a constant separation $L = 50$ nm. The circles and dashed curves are obtained from simulation and the model, respectively. The sizes of the circles represent the relative height of each peak. The black horizontal and vertical dashed lines are the constant central frequency of two modes with same symmetry and the constant frequency difference of two modes with same chirality, respectively, as predicted by the model. The inset shows the values of κ_x and κ_y.

ison, we present the corresponding extinction spectrum as $B = 0$ T in Fig. 6(a). Although being contacted at a point, the excitation of y polarization keeps the same behavior as that of the above well-separated cases, e.g., dominated by a resonance peak consisting of two vertical dipoles. However, the excitation of x polarization is quite distinct. In addition to the resonance peak at point b (two horizontal dipoles), there is a new one at point a, which exhibits a completely different field pattern (see the inset). The corresponding resonance is seen as a strong dipole contributed by two nanodisks and an opposite and weak dipole confined at the touching point. We can image the two nanodisks forming a coherent whole, as
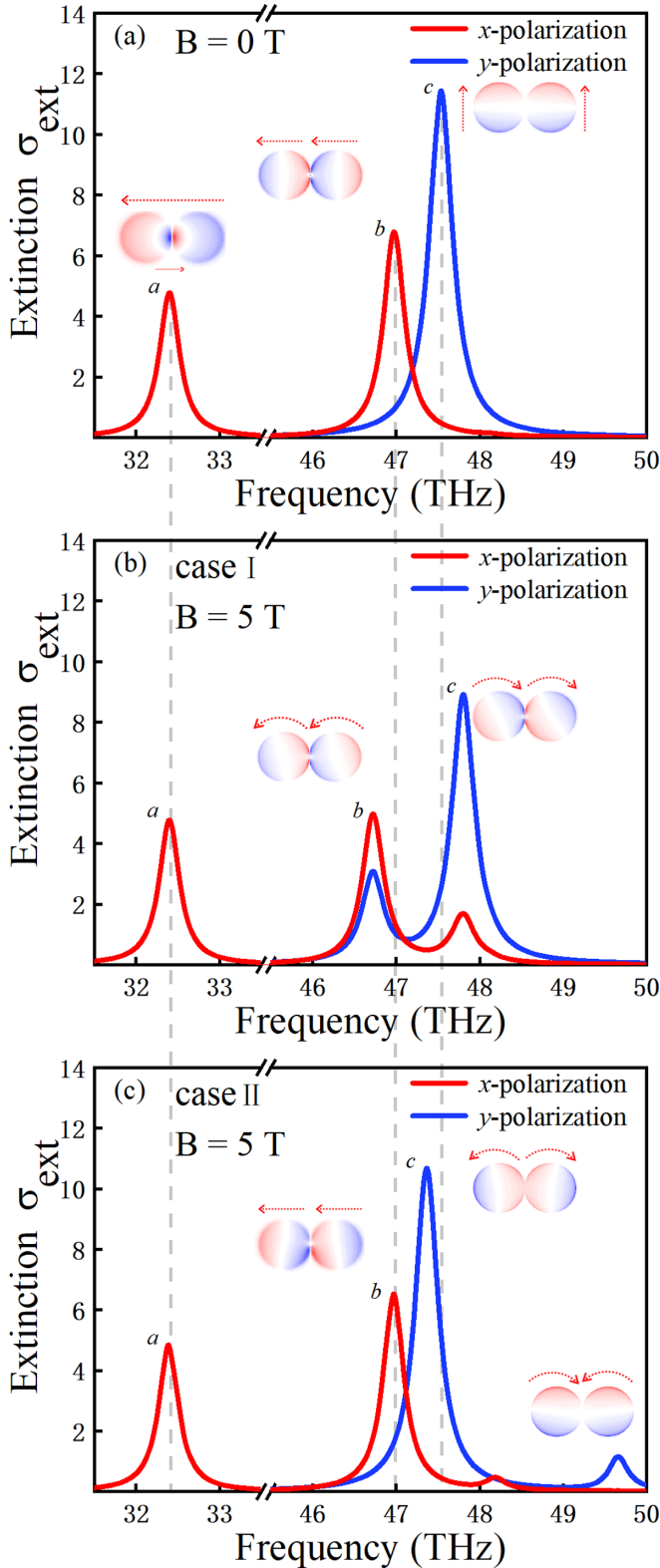
FIG. 6. Extinction spectra of the touching nanodisks for different cases. The insets show the field patterns of modes *a*, *b*, and *c*. The three dotted curves mark the frequencies of the three modes as B = 0 T. The frequency and field pattern of mode *a* is conserved in three situations and those of mode *b* as B = 0 T and in case II.

bridged by the current flowing through the touching point. This indicates the charge transfer effect appears to determine this mode, which thus is usually termed a charge transfer plasmon (CTP) [60–62]. It is obvious that, because of their different mechanisms, modes *a*, *b*, and *c* will show diverse magneto-optic effects.

As shown in Figs. 6(b) and 6(c), the resonance frequency and wave pattern of the CTP mode are reserved, in both cases I and II. It seems the magneto-optic effect is totally suppressed, which has been demonstrated in narrow graphene rectangles [42], due to the lack of mode degeneracy. However, modes *b* and *c* will show different variations in cases I and II. In case I, mode *b* exhibits a redshift, while there is a blueshift for mode *c*. Their wave functions are the linear combinations of two waves of either RHCP or LHCP. It is easy to find that the behavior is identical to that shown in Fig. 2(b), which means there is no significant effect caused by the touching point, only at quantitative level. In case II, mode *c* (*y* polarization) also undergoes a similar redshift and carries a similar wave function, as compared with Fig. 2(c). Nevertheless, mode *b* with its polarization parallel to the touching direction shows roughly the same resonance frequency as that in the absence of a magnetic field (see the dashed line), and its wave function is a linear combination of two linear states rather than circular states. Obviously, it is another suppression of the magneto-optic effect yet different from that in CTP, as clearly seen from their wave functions. The suppression here seems to be very obscure and hard to understand. At least one will be curious about why it only happens for *x* polarization, and if so, why it does not happen for *x* polarization in case I? The circular edge current caused by cyclotron resonance of electrons is the key to understanding the behavior, which is also a typical label of the magneto-optic effect in confined systems [39,47]. For CTP, no circular edge currents are involved, and thus, no magneto-optic effect will appear. In case I, although edge currents are present in each nanodisk, because of the same rotation direction, they will cancel out at the touching point for both polarizations, which means no edge currents are required for the magneto-optic effect in this case. In case II, because of the different rotation directions of edge current in each nanodisk, a *y*-direction edge current flowing through the touching point is required to maintain the magneto-optic effect here. For *y* polarization, the incident electric field is along the *y* direction as well, and hence, the *y*-direction edge current at the touching point will be preserved and consequently the magneto-optic effect. However, for *x* polarization, the *y*-direction edge current at the touching point will be destroyed by the incident electric field along the touching direction. As a result, even in the presence of a magnetic field, no frequency shift appears, and the wave function is a combination of two linear states.

IV. CONCLUSIONS

To conclude, we theoretically investigate MPC in graphene nanodisk dimers, which as we know, is not well understood to date. The fundamental states are circularly polarized MPs caused by the magneto-optic effect rather than plasmons of linear polarization for which the coupling has been studied intensively. We find that, like usual plasmonic coupling, MPC
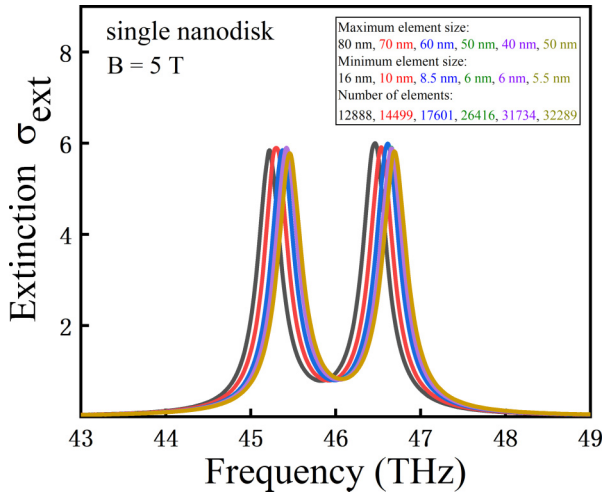
FIG. 7. Convergence test of the simulations of a single graphene nanodisk as $B = 5$ T. The colored curves are obtained by using different mesh setting, which are converged as maximum/minimum element sizes <50 and 6 nm, respectively.

also appears for the two states with the same polarization, e.g., between RHCP/LHCP and RHCP/LHCP, respectively. Here, the chirality is determined by the direction of cyclotron resonance, namely, the external magnetic field. The excitation of specific MPC depends on the polarization of the incident wave; generally, only two symmetric modes can be excited in case I, while in case II, none of the symmetric and antisymmetric modes are dark. Inspired by the perturbation theory of two coupled linear oscillators (2×2 Hamiltonian), we treat MPC of two circular oscillators by directly incorporating the magneto-optic effect, which results in an extended 4×4 Hamiltonian. The crucial point here is the decomposition of each circular oscillator as two orthogonal linear oscillators yet with a $\pi/2$ phase difference. Intuitively, they are connected by the magneto-optic effect (the parameter β) in each nanodisk, and between two nanodisks, their interactions are described by the straight dipole-dipole coupling (the parameters κ_x and κ_y). All these parameters can be extracted from simulations independently and before MPC investigations. To diagonalize the extended Hamiltonian, we show the resonance frequencies of the MPC systems, which are in very good agreement with
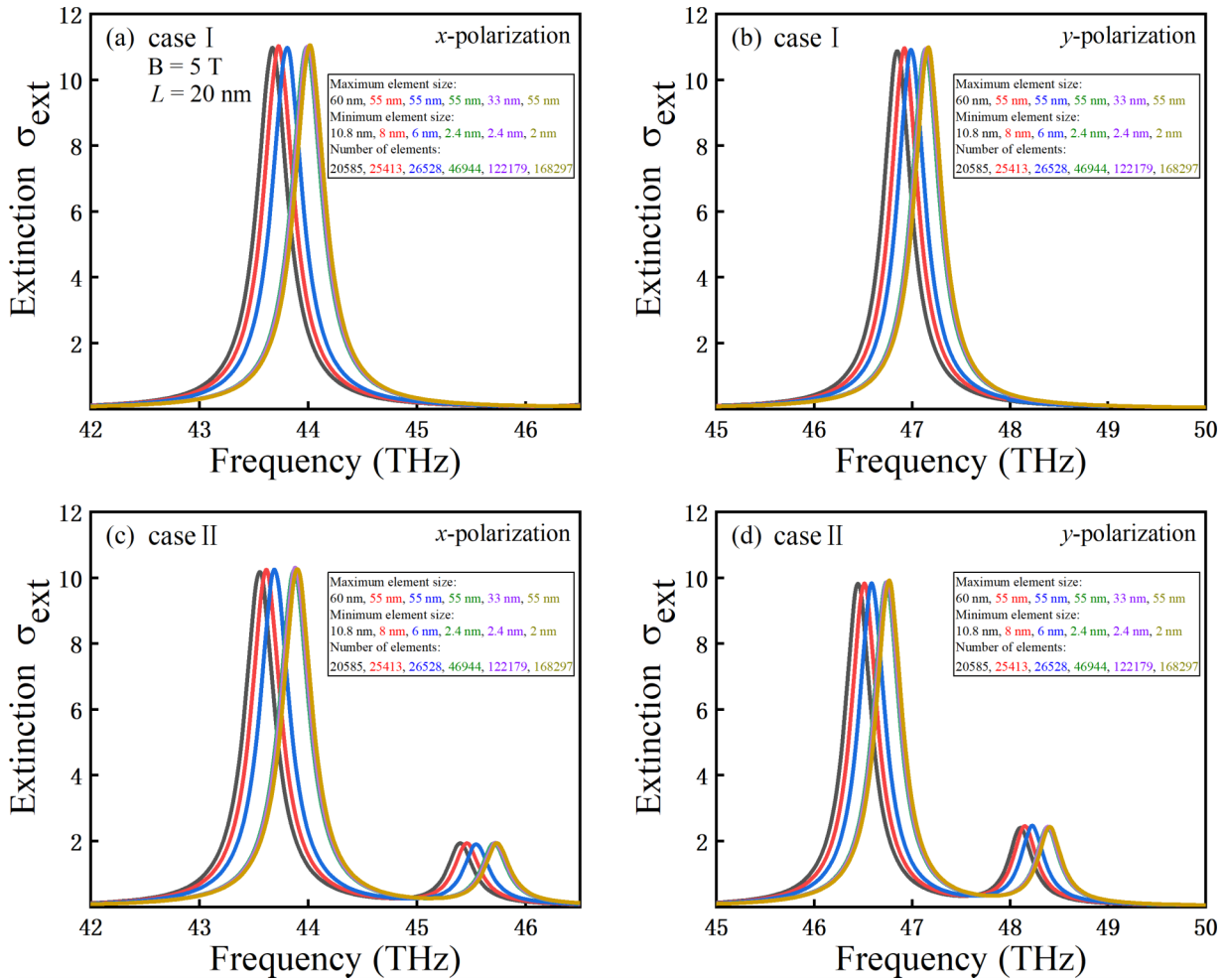

FIG. 8. Convergence test of the simulations of a graphene nanodisk dimer as the separation $L = 20$ nm and $B = 5$ T. The colored curves are obtained by using different mesh setting. For all situations, the convergence results are achieved as maximum/minimum element sizes <55 and 2.4 nm, respectively.
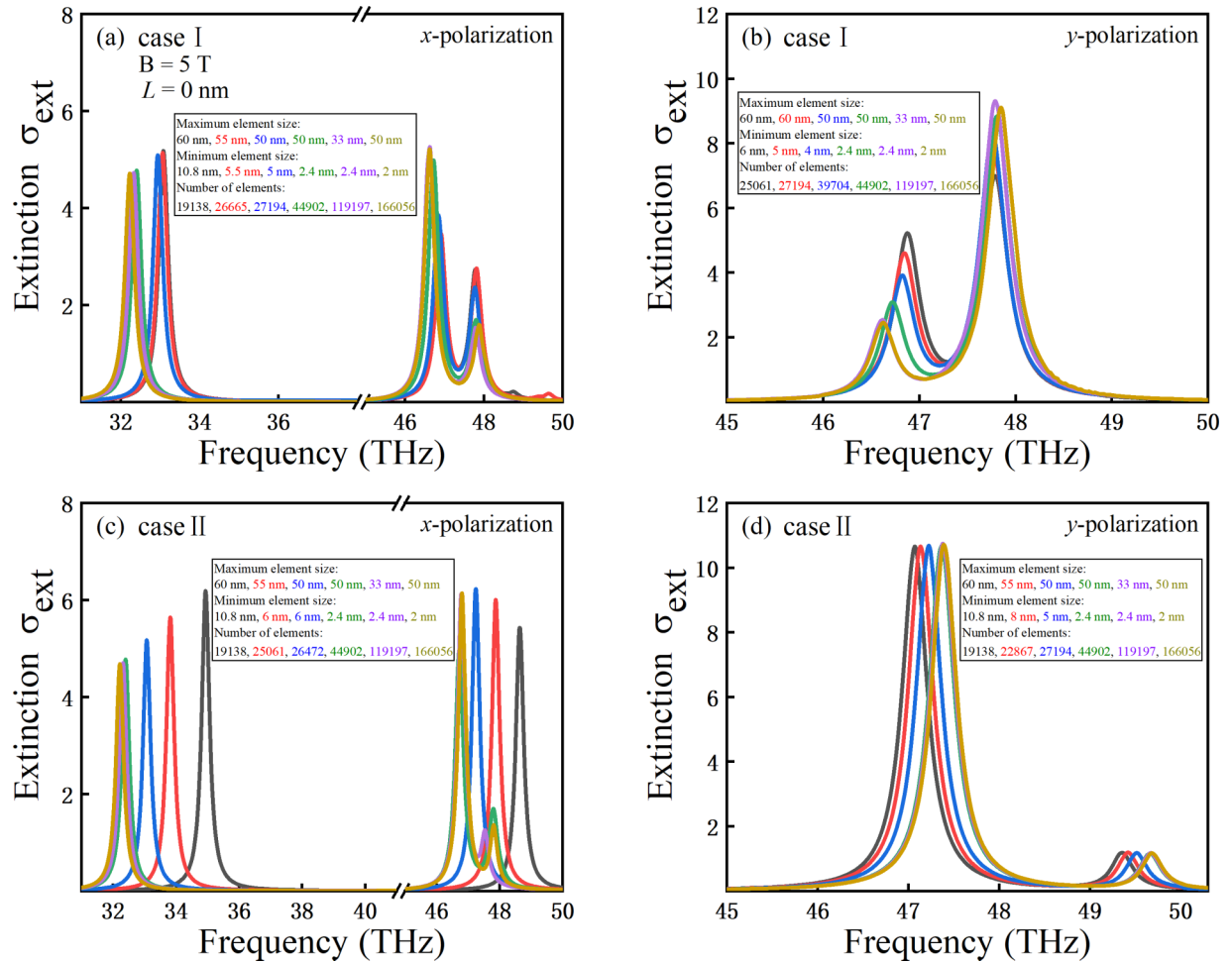
FIG. 9. Convergence test of the simulations of a graphene nanodisk touching dimer ($L = 0$ nm) as $B = 5$ T. The curves of different colors correspond to different mesh setting. For all situations, the dominate peaks are converged as maximum/minimum element sizes <50 and 2.4 nm, respectively.

those from simulations. Moreover, the resonance strength of each mode can be well predicted by the wave functions. Finally, we study MPC in a limited case of a dimer, namely, touching nanodisks. The CTP appears at a lower frequency, which is immune to the magneto-optic effect. In case II, under x-polarized excitation, the circular motion of MPs will also be suppressed. In this paper, we push forward the fundamental understanding of MPC in graphene nanostructures, which should be generally valid in other 2D materials, and pave the way for magneto-optical and plasmonic applications.

APPENDIX: CONVERGENCE ANALYSIS OF NUMERICAL SIMULATIONS

In this Appendix, we provide detailed convergence analysis of numerical simulations. Because of the artificial thickness ($t_g = 0.5$ nm) of graphene nanodisks, fine meshing is generally required, and the simulations are rather memory and

time consuming. In practice, we mesh the computational domain by using tetrahedral elements adapted for the physics settings of the model, where the smaller (larger) elements are generated close to (away from) graphene. The meshing can be further specified by two built-in variables, maximum/minimum element sizes. Through reducing either one of them, the total number of elements will increase, which in principle will lead to a more accurate result, offering a feasible way to check numerical convergence. Below, we check convergence of several typical simulations, e.g., those carried out for producing Figs. 2 and 6 in the main text. Note that the radius of the graphene nanodisk is 50 nm, and the radius of the spherical computational domain is 300 nm. For convenience, the mesh setting used in the main text is indicated by the green curve in all figures.

In fact, for a single graphene nanodisk, it is not that difficult to achieve convergence. As shown in Fig. 7, with increasing the number of elements, the change of the extinction spectrum of a single graphene nanodisk gets slower and slower. When the maximum/minimum element sizes are reduced to 50 and 6 nm, respectively, the number of elements reaches 26 416 (green curve), and then the result exhibits very high accuracy. With further decreasing maximum or minimum element size

(purple and dark yellow curves, respectively), it is seen that they nearly coincide with the green curve.

For the dimer of a finite separation, e.g., $L = 20$ nm, much more elements should be used, and the convergence test is summarized in Fig. 8. The optimal maximum/minimum element sizes are 55 and 2.4 nm, respectively, and the number of elements is 46 944 (green curve). If further decreasing maximum/minimum element sizes, e.g., the purple and dark yellow curves, respectively, the result remains almost unchanged, clear evidence of convergence. Another important feature is, for this dimer, the convergence will be reached simultaneously in cases I and II and does not depend on the polarization.

The simulations of a touching dimer should be carried out more carefully. Comparing the simulations of the dimer with separation $L = 20$ nm (the above case), the maximum element size should be reduced. The convergence test is shown in Fig. 9. It is seen that, as maximum/minimum element sizes are set to be 50 and 2.4 nm, respectively, the number of elements is 44 902 (green curve). The result with reasonable accuracy is obtained. With decreasing maximum/minimum element sizes (purple and dark yellow curves, respectively), it is easy to find that the main resonance peaks remain almost unchanged, and two minor peaks in Figs. 9(b) and 9(c) change slightly. However, since our discussion focuses mostly on the main peaks, this meshing is quite acceptable.

---

[1] D. K. Gramotnev and S. I. Bozhevolnyi, Nat. Photon. **4**, 83 (2010).

[2] J. A. Schuller, E. S. Barnard, W. Cai, Y. Ch. Jun, J. S. White, and M. L. Brongersma, Nat. Mater. **9**, 193 (2010).

[3] S. Kawata, Y. Inouye, and P. Verma, Nat. Photon. **3**, 388 (2009).

[4] E. Ozbay, Science **311**, 189 (2006).

[5] Q. Bao and K. P. Loh, ACS Nano **6**, 3677 (2012).

[6] S. H. Lee, M. Choi, T.-T. Kim, S. Lee, M. Liu, X. Yin, H. K. Choi, S. S. Lee, C.-G. Choi, S.-Y. Choi, X. Zhang, and B. Min, Nat. Mater. **11**, 936 (2012).

[7] K. S. Novoselov, A. K. Geim, S. V. Morozov, D. Jiang, Y. Zhang, S. V. Dubonos, I. V. Grigorieva, and A. A. Firsov, Science **306**, 666 (2004).

[8] F. H. L. Koppens, D. E. Chang, and F. J. García de Abajo, Nano Lett. **11**, 3370 (2011).

[9] J. Chen, M. Badioli, P. Alonso-González, S. Thongrattanasiri, F. Huth, J. Osmond, M. Spasenovic, A. Centeno, A. Pesquera, P. Godignon, A. Z. Elorza, N. Camara, F. J. García de Abajo, R. Hillenbrand, and F. H. L. Koppens, Nature (London) **487**, 77 (2012).

[10] Z. Fei, A. S. Rodin, G. O. Andreev, W. Bao, A. S. McLeod, M. Wagner, L. M. Zhang, Z. Zhao, M. Thiemens, G. Dominguez, M. M. Fogler, A. H. Castro Neto, C. N. Lau, F. Keilmann, and D. N. Basov, Nature (London) **487**, 82 (2012).

[11] A. H. Castro Neto, F. Guinea, N. M. R. Peres, K. S. Novoselov, and A. K. Geim, Rev. Mod. Phys. **81**, 109 (2009).

[12] F. Bonaccorso, Z. Sun, T. Hasan, and A. C. Ferrari, Nat. Photon. **4**, 611 (2010).

[13] G. X. Ni, L. Wang, M. D. Goldflam, M. Wagner, Z. Fei, A. S. Mcleod, M. K. Liu, F. Keilmann, B. Özyilmaz, and A. H. C. Neto, Nat. Photon. **10**, 244 (2016).

[14] Y. D. Kim, H. Kim, Y. Cho, J. H. Ryoo, C.-H. Park, P. Kim, Y.-S. Kim, S. Lee, Y. Li, S.-N. Park, Y.-S. Yoo, D. Yoon, V. E. Dorgan, E. Pop, T. F. Heinz, J. Hone, S.-H. Chun, H. Cheong, S. W. Lee, M.-Ho Bae *et al.*, Nat. Nanotechnol. **10**, 676 (2015).

[15] A. N. Grigorenko, M. Polini, and K. S. Novoselov, Nat. Photon. **6**, 749 (2012).

[16] W. G. Liu, B. Hu, Z. D. Huang, H. Y. Guan, H. T. Li, X. K. Wang, Y. Zhang, H. X. Yin, X. L. Xiong, J. Liu, and Y. T. Wang, Photon. Res. **6**, 703 (2018).

[17] J. S. Gomez-Diaz and A. Alù, ACS Photon. **3**, 2211 (2016).

[18] B. Radisavljevic, A. Radenovic, J. Brivio, V. Giacometti, and A. Kis, Nat. Nanotechnol. **6**, 147 (2011).

[19] Q. H. Wang, K. Kalantar-Zadeh, A. Kis, J. N. Coleman, and M. S. Strano, Nat. Nanotechnol. **7**, 699 (2012).

[20] L. Li, Y. Yu, G. J. Ye, Q. Ge, X. Ou, H. Wu, D. Feng, X. H. Chen, and Y. Zhang, Nat. Nanotechnol. **9**, 372 (2014).

[21] B. Luk'yanchuk, N. I. Zheludev, S. a Maier, N. J. Halas, P. Nordlander, H. Giessen, and C. T. Chong, Nat. Mater. **9**, 707 (2010).

[22] D. DeJarnette, J. Norman, and D. K. Roper, Photon. Res. **2**, 15 (2014).

[23] F. Hao, Y. Sonnefraud, P. V. Dorpe, S. A. Maier, N. J. Halas, and P. Nordlander, Nano Lett. **8**, 3983 (2008).

[24] M. Fleischhauer, A. Imamoglu, and J. P. Marangos, Rev. Mod. Phys. **77**, 633 (2005).

[25] K.-J. Boller, A. Imamoğlu, and S. E. Harris, Phys. Rev. Lett. **66**, 2593 (1991).

[26] S. Zhang, D. A. Genov, Y. Wang, M. Liu, and X. Zhang, Phys. Rev. Lett. **101**, 047401 (2008).

[27] S. Romano, G. Zito, S. Torino, S. Cabrini, I. Rendina, G. Coppola, G. Calafiore, E. Penzo, and V. Mocella, Photon. Res. **6**, 726 (2018).

[28] C. W. Hsu, B. Zhen, A. D. Stone, J. D. Joannopoulos, and M. Soljacic, Nat. Rev. Mater. **1**, 16048 (2016).

[29] D. C. Marinica, A. G. Borisov, and S. V. Shabanov, Phys. Rev. Lett. **100**, 183902 (2008).

[30] T. Atay, J.-H. Song, and A. V. Nurmikko, Nano Lett. **4**, 1627 (2004).

[31] J. B. Lassiter, J. Aizpurua, L. I. Hernandez, D. W. Brandl, I. Romero, S. Lal, J. H. Hafner, P. Nordlander, and N. J. Halas, Nano Lett. **8**, 1212 (2008).

[32] J. D. Cox, M. R. Singh, G. Gumbs, M. A. Antón, and F. Carreño, Phys. Rev. B **86**, 125452 (2012).

[33] F. Liu, A. V. Rodina, D. R. Yakovlev, A. A. Golovatenko, A. Greilich, E. D. Vakhtin, A. Susha, A. L. Rogach, Y. G. Kusrayev, and M. Bayer, Phys. Rev. B **92**, 125403 (2015).

[34] Y. He, M. Maciejczyk, S. Ołdziej, H. A. Scheraga, and A. Liwo, Phys. Rev. Lett. **110**, 098101 (2013).

[35] K. S. Novoselov, Z. Jiang, Y. Zhang, S. V. Morozov, H. L. Stormer, U. Zeitler, J. C. Maan, G. S. Boebinger, P. Kim, and A. K. Geim, Science **315**, 1379 (2007).

[36] S. Murakami, N. Nagaosa, and S.-C. Zhang, Science **301**, 1348 (2003).

[37] F. Guinea, M. I. Katsnelson, and A. K. Geim, Nat. Phys. **6**, 30 (2010).

[38] M. J. Lea and M. I. Dykman, Physica B **249**, 628 (1998).

[39] W. Wang, S. P. Apell, and J. M. Kinaret, Phys. Rev. B **86**, 125450 (2012).

[40] I. Crassee, M. Orlita, M. Potemski, A. L. Walter, M. Ostler, Th. Seyller, I. Gaponenko, J. Chen, and A. B. Kuzmenko, Nano Lett. **12**, 2470 (2012).

[41] H. Yan, Z. Li, X. Li, W. Zhu, P. Avouris, and F. Xia, Nano Lett. **12**, 3766 (2012).

[42] N. Jiao, S. Kang, K. Han, X. Shen, and W. Wang, Phys. Rev. B **99**, 195447 (2019).

[43] T. G. Pedersen, Phys. Rev. B **103**, 085419 (2021).

[44] N. Jiao, S. Kang, K. Han, X. Shen, and W. Wang, Phys. Rev. B **103**, 085405 (2021).

[45] W. Wang, T. Christensen, A.-P. Jauho, K. S. Thygesen, M. Wubs, and N. A. Mortensen, Sci. Rep. **5**, 9535 (2015).

[46] W. Wang and J. M. Kinaret, Phys. Rev. B **87**, 195424 (2013).

[47] W. Wang, J. M. Kinaret, and S. P. Apell, Phys. Rev. B **85**, 235444 (2012).

[48] M. Orlita, C. Faugeras, R. Grill, A. Wysmolek, W. Strupinski, C. Berger, W. A. de Heer, G. Martinez, and M. Potemski, Phys. Rev. Lett. **107**, 216603 (2011).

[49] K. Horii, T. Nakasuga, T. Hirahara, S. Tajima, R. Ebisuoka, K. Watanabe, T. Taniguchi, and R. Yagi, Phys. Rev. B **100**, 245420 (2019).

[50] S. Kim, I. Jo, D. C. Dillen, D. A. Ferrer, B. Fallahazad, Z. Yao, S. K. Banerjee, and E. Tutuc, Phys. Rev. Lett. **108**, 116404 (2012).

[51] D. Jin, Y. Xia, T. Christensen, M. Freeman, S. Wang, K. Y. Fong, G. C. Gardner, S. Fallahi, Q. Hu, Y. Wang, L. Engel, Z.-L. Xiao, M. J. Manfra, N. X. Fang, and X. Zhang, Nat. Commun. **10**, 4565 (2019).

[52] A. B. Evlyukhin, T. Fischer, C. Reinhardt, and B. N. Chichkov, Phys. Rev. B **94**, 205434 (2016).

[53] M. J. Berg, C. M. Sorensen, and A. Chakrabarti, J. Opt. Soc. Am. A **25**, 1504 (2008).

[54] A. Samanta, Sk. M. Ali, and S. K. Ghosh, Phys. Rev. Lett. **92**, 145901 (2004).

[55] B. Deng, Q. Guo, C. Li, H. Wang, X. Ling, D. B. Farmer, S.-J. Han, J. Kong, and F. Xia, ACS Nano **10**, 11172 (2016).

[56] W. Xiao, Y. Chen, K. Han, X. Shen, and W. Wang, Phys. Rev. Applied **13**, 014029 (2020).

[57] C. Qu, S. Ma, J. Hao, M. Qiu, X. Li, S. Xiao, Z. Miao, N. Dai, Q. He, S. Sun, and L. Zhou, Phys. Rev. Lett. **115**, 235503 (2015).

[58] S. Thongrattanasiri, F. H. L. Koppens, and F. J. García de Abajo, Phys. Rev. Lett. **108**, 047401 (2012).

[59] J. Lin, M. Qiu, X. Zhang, H. Guo, Q. Cai, S. Xiao, Q. He, and L. Zhou, Light Sci. Appl. **9**, 158 (2020).

[60] F. Wen, Y. Zhang, S. Gottheim, N. S. King, Y. Zhang, P. Nordlander, and N. J. Halas, ACS Nano **9**, 6428 (2015).

[61] V. Kulkarni and A. Manjavacas, ACS Photon. **2**, 987 (2015).

[62] Y. Wang, Z. Li, K. Zhao, A. Sobhani, X. Zhu, Z. Fang, and N. J. Halas, Nanoscale **5**, 9897 (2013).